Available online at www.sciencedirect.com
ScienceDirect
Trans. Nonferrous Met. Soc. China 35(2025) 2227−2243
Transactions of Nonferrous Metals Society of China
www.tnmsc.cn

# Microstructure evolution and strengthening mechanism of WE54 magnesium alloy during hard-plate rolling

Yan-hui LIU[1], Ming-ming QI[2], Xin CAO[1], Bing WU[1], Ming LIANG[1], Jian-feng LI[1], Chao LI[1]

1. Institute of Magnesium and Lithium Materials, Northwest Institute for Nonferrous Metal Research, Xi'an 710016, China;
2. School of Materials Science and Engineering, Xi'an University of Technology, Xi'an 710048, China

Received 13 November 2023; accepted 3 June 2024

**Abstract:** The microstructure evolution and strengthening mechanism of WE54 alloy with different hard-plate rolling (HPR) processes were systematically investigated. The results suggest that the mechanical properties of the as-rolled alloys are significantly enhanced compared to those of the as-cast alloy. When subjected to three rolling passes at 450 °C and 490 °C, grain refinement occurs due to dynamic recrystallization. A mixed-grain structure is formed after a single pass rolling with a substantial reduction (65%) at 490 °C. The dynamic recrystallization (DRX) mechanism of the alloy during the HPR includes continuous dynamic recrystallization (CDRX), discontinuous dynamic recrystallization (DDRX), and twin-induced recrystallization (TDRX). The WE54 alloy exhibits the highest strength after three passes of HPR at 450 °C, with tensile strength and yield strength of 374 and 323 MPa, respectively. The significant improvement in the mechanical properties of the alloy is primarily attributed to fine-grain strengthening, solid solution strengthening, and dislocation strengthening.

**Key words:** WE54 alloy; hard-plate rolling (HPR); microstructure; mechanical properties; strengthening mechanism

## 1 Introduction

Magnesium alloys are used in aerospace, defence, and military industries due to their low density, high specific strength and stiffness, and high electromagnetic shielding properties [1,2]. In recent years, the increased demand for lightweight equipment has further accelerated the development of magnesium alloys. However, their large-scale applications are limited by their relatively poor strength compared to traditional metal structural materials such as steel and aluminium alloys [3−5].

Among the various wrought magnesium alloys (e.g., AZ series, ZK series, Mg−RE series, etc.), Mg−RE alloys have attracted significant attention due to their outstanding mechanical properties, such as WE54 (Mg−5.1Y−3.3RE−0.5Zr, wt.%) and WE43 (Mg−4.2Y−3.3RE−0.5Zr, wt.%) magnesium alloys [6,7]. The tensile strength (UTS), yield strength (TYS), and elongation of WE54 alloy at room temperature are 285 MPa, 200 MPa, and 4%, respectively, which is still far from the aluminium alloys in terms of mechanical properties [8]. To enhance the mechanical properties of WE54 alloy, researchers have explored various strategies, including compositional adjustments such as increasing the content of alloying elements and introducing new alloying elements. LI et al [9] improved the mechanical properties of Mg−5.10Y−

**Corresponding author:** Yan-hui LIU, Tel: +86-13679176975, E-mail: liuyanhuiLYH1016@163.com;
Ming LIANG, Tel: +86-13991212996, E-mail: mliang@c-nin.com
https://doi.org/10.1016/S1003-6326(25)66811-7

1.91Nd−2.03Gd (wt.%) alloy by utilizing the grain refining effects of Zr elements. GUI et al [10] introduced 3 wt.% Sm elements in Mg−5Y−2Nd−0.5Zr alloy, which increased compressive strength of up to 390 MPa. This improvement is attributed to the grain refining effect of the Sm element. TIAN et al [11] enhanced the tensile strength of WE54 alloy to 302 MPa by adjusting the elemental content of Gd and combining it with ageing treatment. Besides compositional regulation, deformation processing (such as extrusion, forging, and rolling) is also an effective method for enhancing the mechanical properties of WE54 alloys. YU et al [8] reported a high-performance Mg−3Y−2Gd−1Nd−0.5Zr (wt.%) alloy using extrusion + rolling + ageing treatment, with tensile strength, yield strength, and elongation of 345 MPa, 301 MPa, and 9%, respectively, which is comparable to the mechanical properties of the 6061Al alloy. OROZCO-CABALLERO et al [12] employed a method combining equal-channel angular pressing (ECAP) and ultrasonic surface rolling processing (USRP) to prepare Mg−2Nd−0.6Y−0.5Zr (wt.%) alloy with fine-grains and high-density dislocations. This process resulted in an increase in the tensile strength of the alloy from 262 to 330 MPa.

Traditional rolling processes often result in edge-cracking due to significant shear stresses along the rolling direction [13]. Hard-plate rolling (HPR) is an upgrade from the conventional rolling method, offering the advantages of reducing edge-cracking, improving rolling efficiency, and effectively improving the mechanical properties of the alloy [14−16]. Inspired by the HPR process, a hard-plate hot forging (HPHF) method was developed, and the microstructure and mechanical properties of magnesium alloys under various HPHF conditions were investigated. The results indicated significant improvements in the mechanical properties of magnesium alloys [17−21]. However, research on HPR was primarily focused on the deformation of RE-free magnesium alloys, with its application in Mg−RE alloys remaining limited.

In this study, HPR was employed to enhance the mechanical properties of the WE54 magnesium alloy. The dynamic recrystallization behaviour and strengthening mechanisms of the WE54 alloy were investigated through analysis of the microstructure evolution with varying rolling temperatures and deformation paths.

## 2 Experimental

The alloy used in this study was the commercial WE54 alloy. The chemical composition of the alloy was examined using inductively coupled plasma−atomic emission spectrometry (ICP−AES), and the obtained results are listed in Table 1. Homogenization heat treatment of the WE54 alloy was undertaken at 520 °C for 8 h, followed by cold water quenching. The plate specimens with dimensions of 40 mm × 25 mm × 4 mm were cut from as-cast alloy. Before rolling, the specimen was fixed between two steel plates using steel wires. The schematic diagram for the HPR of the WE54 alloys is presented in Fig. 1(a). The HPR processes for different alloys are illustrated in Fig. 1(c). Each specimen was held at the rolling temperature for 20 min before rolling. For S1 and S2 alloys, the rolling reduction between passes was 30%, and the total thickness reduction was 65%. Each specimen was annealed for 15 min to eliminate residual stresses. The S3 alloy was HPRed in a single pass with a thickness reduction of 65% at a temperature of 490 °C. The surfaces of the final rolled specimens were smooth and bright, as shown in Fig. 1(b), and no cracks were found on the edges, indicating that HPR can improve the formability of the WE54 alloy.

**Table 1** Chemical composition of WE54 alloy (wt.%)

| Y | Nd | Gd | Zr | Mg |
|---|---|---|---|---|
| 5.03 | 2.02 | 1.30 | 0.37 | Bal. |

The room-temperature tensile properties of specimens with a width of 4 mm and a gauge length of 20 mm were tested with an initial strain rate of 0.2 mm/min at ambient temperature. Three tensile experiments were conducted for each alloy, and the mean values were taken as the final mechanical properties. The microstructure was examined using optical microscopy (OM, Olympus BX51), with grain size determined via the linear intercept method from optical micrographs. Metallographic samples were prepared by grinding, polishing, and etched in a solution of 4.2 g picric acid, 10 mL acetic acid, 70 mL ethanol, and 10 mL distilled water. A scanning electron microscope (SEM, Hitachi SU5000) equipped with an electron backscattered diffraction (EBSD) detector was used

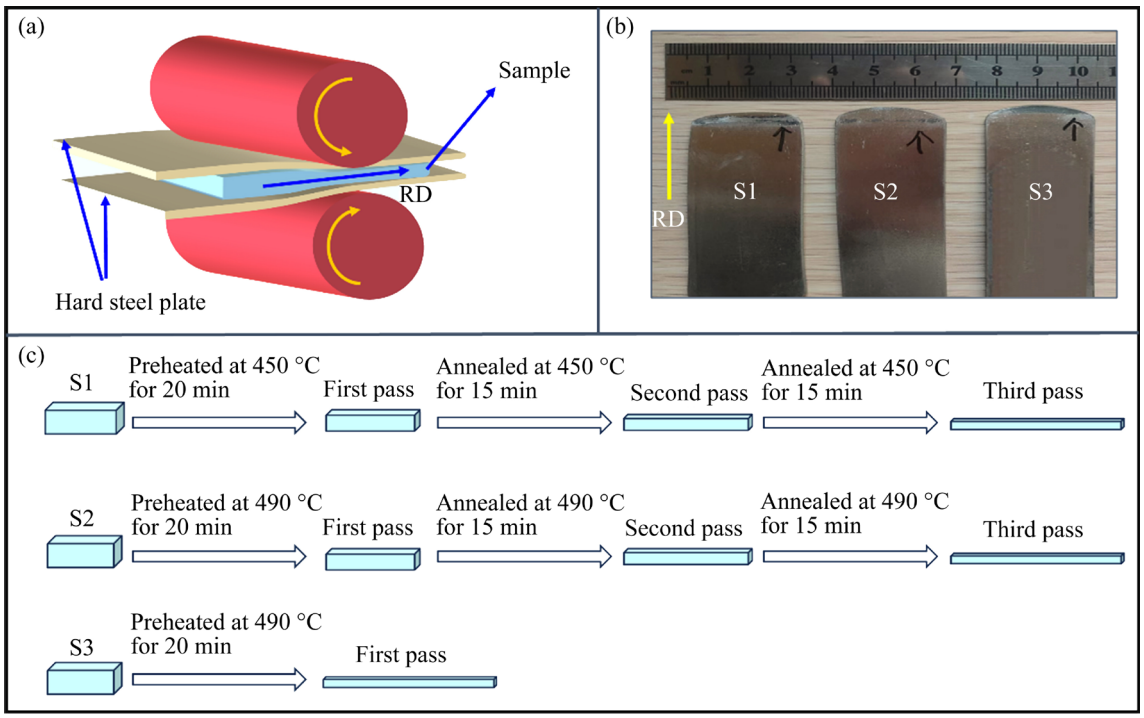


**Fig. 1** Schematic diagram of HPR for WE54 alloy (a); Appearance of as-rolled alloys (b); Schematic diagrams of HPR process routes for S1, S2, S3 samples (c)

to examine the microstructure. The specimens for EBSD observation were electrochemically polished in a solution of 15 mL perchloric acid and 85 mL alcohol at 25 V and 0.5 mA for 5−8 s. The data were analyzed using Channel 5 software. Additionally, detailed microstructure was investigated on a transmission electron microscope (JEOL, JEM−F200). Thin foils for the TEM observation were prepared by mechanical grinding (~50 μm) and ion beam thinning.

## 3 Results

### 3.1 Microstructure evolution

The microstructures of the as-cast and homogenized WE54 alloys are presented in Fig. 2. The as-cast WE54 alloy comprises an $\alpha$-Mg matrix and irregular interdendritic phase located at grain boundaries. Alloy grains are equiaxed with a size of about 70−80 μm. In addition to the eutectic phase at the grain boundaries (e.g., Points B, C, and D in Fig. 2(b)), a small number of cubic phases (e.g., Point A in Fig. 2(b)) as well as particulate phases (e.g., Point E in Fig. 2(b)) are observed in the alloy. According to the results given in Table 2, the cubic phase is enriched with a large amount of Y elements, indicating that the phase is $Mg_{24}Y_5$. The eutectic phase is mainly enriched with Y and Nd elements, and the atomic ratio of Nd to Y is close to 2:1, which suggests that this phase is the $Mg_{14}Nd_2Y$. It is in agreement with the previous reports [22−24]. As for the particle-like phase, the results indicate that it is the $\alpha$-Zr core, consistent with other reports [25−27]. Most of the magnesium alloys are grain-refined by Zr elements. Zr is an ideal heterogeneous nucleation site due to the low crystallographic disregistry between Zr particles and the Mg matrix [27,28]. Figure 2(c) shows the optical image of the homogenized alloy. The eutectic phase located at the grain boundaries has completely dissolved into the matrix, while some petal-like regions are observed inside grains (as shown by the yellow curves in Figs. 2(c, d)). As the petal-like phase is very fine, verifying it with XRD and TEM is necessary. In addition, Table 2 gives the concentrations of Y, Gd, and Nd elements at Point F in Fig. 2(d), and it is clear that Y, Gd, and Nd elements are mainly soluble in the matrix.

Figure 3 displays the XRD patterns of the as-cast and homogenized WE54 alloys. In addition to $\alpha$-Mg, the $Mg_{24}Y_5$ and $Mg_{14}Nd_2Y$ phases are observed for the as-cast alloy, corresponding to the

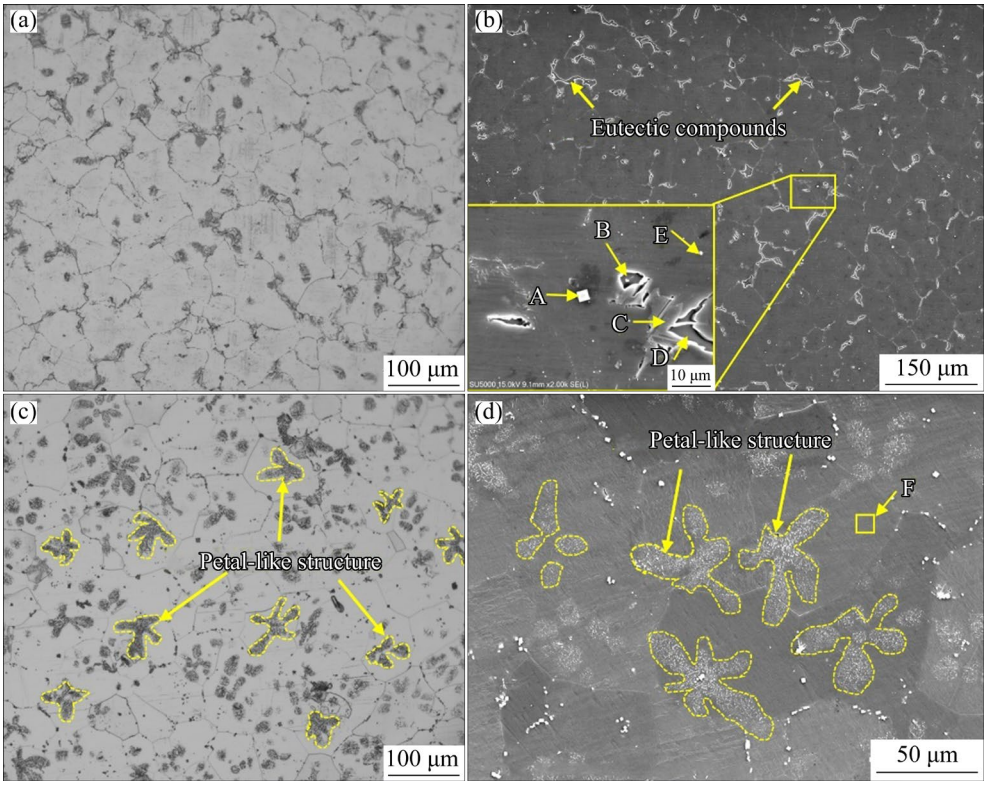


**Fig. 2** Microstructures of as-cast and homogenized WE54 alloys: (a) Optical image of as-cast alloy; (b) SEM image of as-cast alloy; (c) Optical image of homogenized alloy; (d) SEM image of homogenized alloy

**Table 2** EDS analysis results of different points in Fig. 2

| Point | Mg | | Y | | Nd | | Gd | | Zr | |
|---|---|---|---|---|---|---|---|---|---|---|
| | wt.% | at. % | wt.% | at. % | wt.% | at. % | wt.% | at. % | wt.% | at. % |
| A | 11.17 | 33.1 | 73.89 | 59.86 | 4.79 | 2.39 | 10.15 | 4.65 | – | – |
| B | 51.39 | 85.13 | 8.46 | 3.83 | 32.94 | 9.19 | 7.21 | 1.85 | – | – |
| C | 75.99 | 93.19 | 14.99 | 5.03 | 4.65 | 0.96 | 4.37 | 0.82 | – | – |
| D | 45.9 | 81.79 | 11.41 | 5.56 | 35.75 | 10.74 | 6.94 | 1.91 | – | – |
| E | 78.93 | 94 | 3.41 | 1.11 | 3.9 | 0.78 | 1.94 | 0.36 | 11.83 | 3.75 |
| F | 91.87 | 98.02 | 4.8 | 1.4 | 2 | 0.36 | 1.33 | 0.22 | – | – |

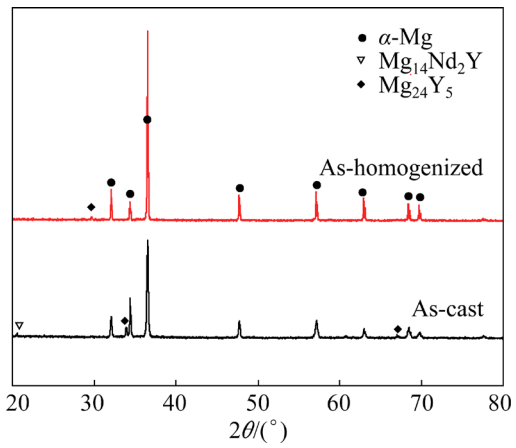


**Fig. 3** XRD patterns of as-cast and as-homogenized WE54 alloys

EDS results. Only the diffraction peaks of Mg are found in the XRD pattern for the as-homogenized alloy, and the petal-like phases need further confirmation.

TEM results for the as-homogenized WE54 alloy are shown in Fig. 4. The high-angle annular dark-field (HAADF) image and elemental maps of the petal-like region in Fig. 4(a) confirm that they consist of rod-shaped phases with different length-to-diameter ratios, and some plate-like phases are also observed. The phase size is in the micron scale. The EDS mapping results confirm that the petal-like regions are enriched with Zr elements. The formation of petal-like regions in

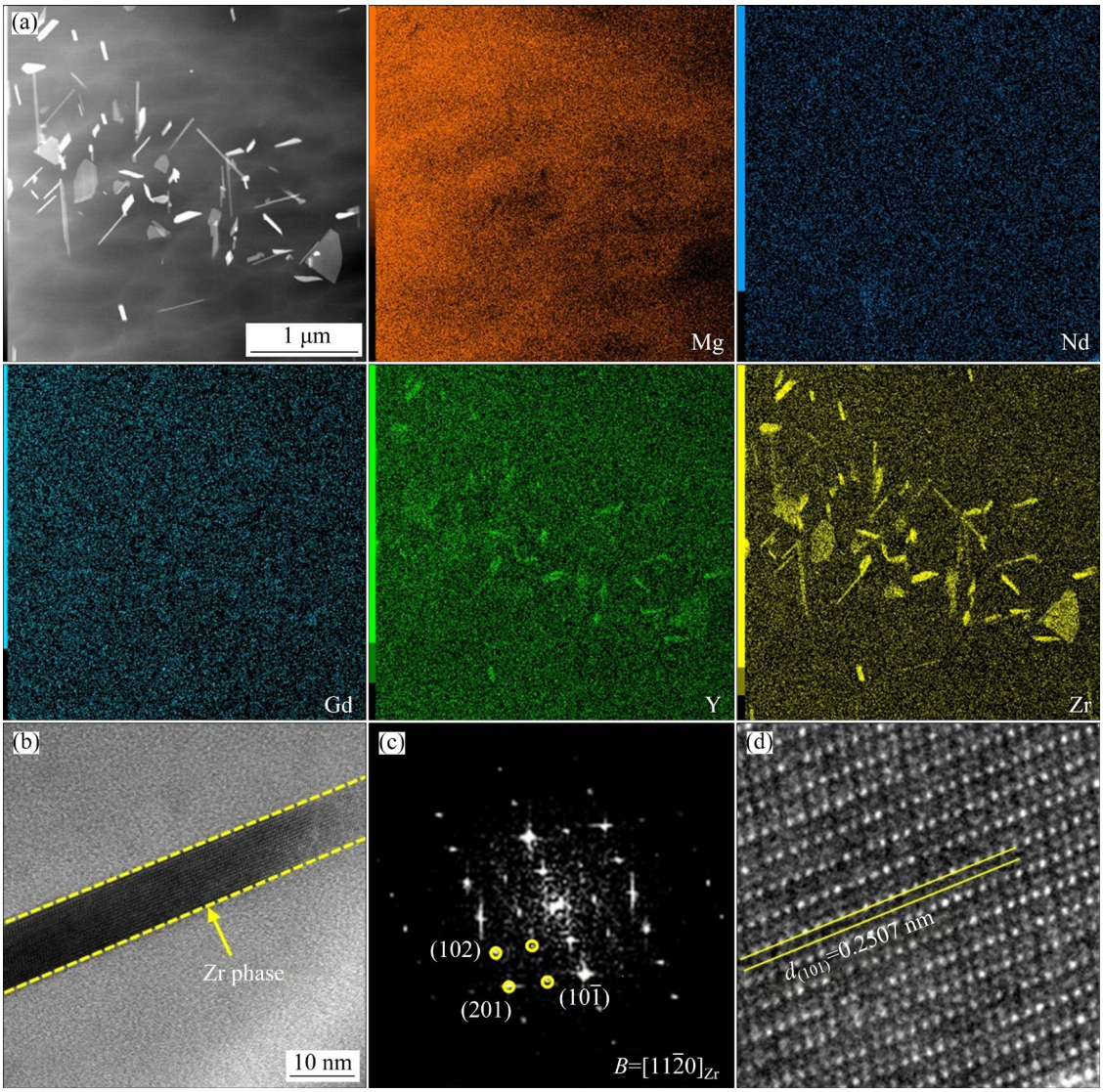


**Fig. 4** TEM results for as-homogenized WE54 alloy: (a) HAADF images of petal-like phase; (b) HRTEM image of rod-like phase; (c) Corresponding FFT image; (d) Corresponding IFFT image

Zr-containing magnesium alloys is very common. ZHANG et al [29] and HU et al [30] observed the petal-like regions in solid-solution-treated Mg−Gd alloys, and the rod-shaped phase was considered to be the Zr-rich phase. This petal-like microstructure has also been found in the Mg−Gd(Nd)−Zn−Zr alloys [31,32], in which the rod-like phase was identified as the $Zn_2Zr_3$ phase in a tetragonal crystal structure. The WE54 alloy studied in this work does not contain Zn elements, so the petal-like microstructure must not be $Zn_2Zr_3$ phase. As determined by high-resolution TEM (HRTEM) and fast Fourier transform (FFT) analysis in Figs. 4(b, c), the rod-like phase is the Zr phase with a hexagonal structure. According to the inverse-FFT (IFFT) analysis, the interplanar distance in $(101)_{Zr}$ is ~0.2507 nm.

Figure 5 shows metallographic photographs of different as-rolled WE54 alloys. When the rolling temperature is 450 °C, with the increase of rolling reduction, the grain size of S1 alloy is gradually refined. After the first and the second passes of rolling, the alloy grain sizes are ~78 μm and ~55 μm, respectively. After three passes of rolling, i.e., when the thickness reduction is 65%, the grain size of the S1 alloy is refined to ~10 μm. At the same time, a small number of deformation twins are observed within the alloy (as shown by the blue arrows in Fig. 5(c)).

When the rolling temperature increases to 490 °C, the grain size of the S2 alloy is gradually refined with the increase of rolling reduction. The

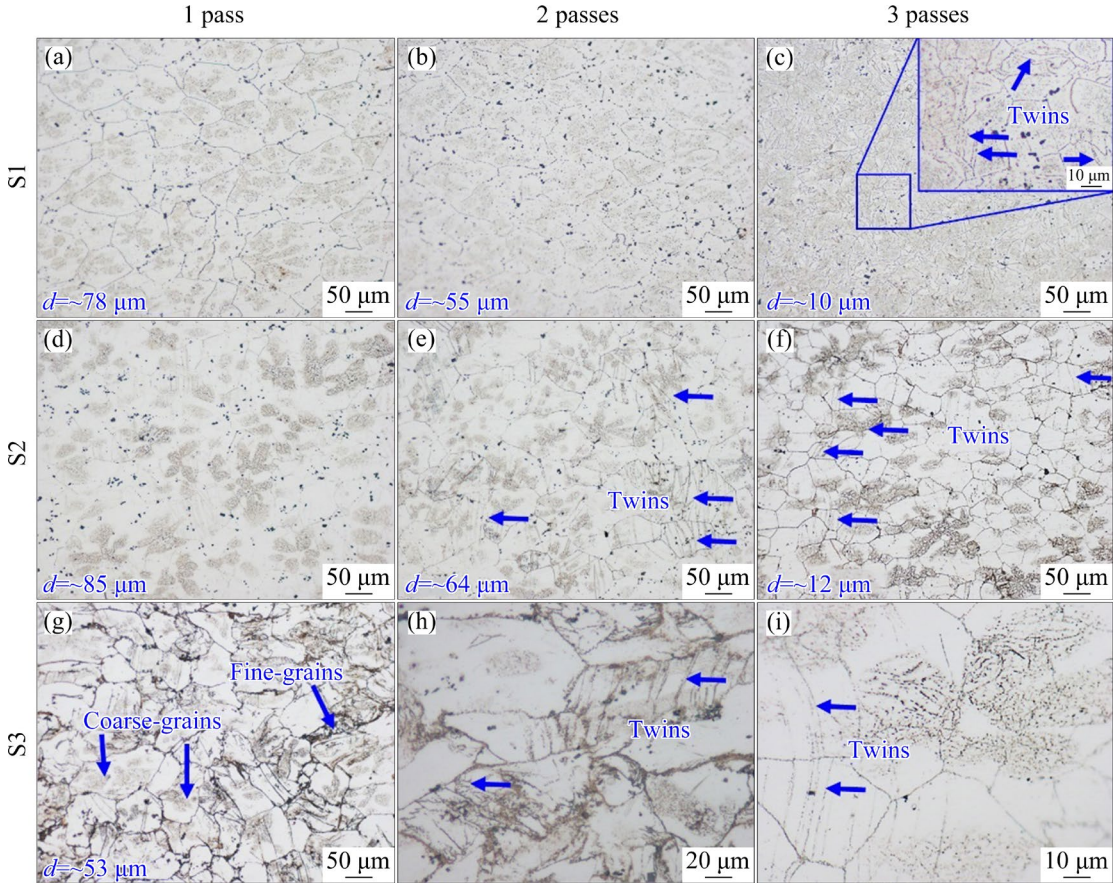


**Fig. 5** Optical micrographs of as-rolled WE54 alloys: (a−c) S1 alloy; (d−f) S2 alloy; (g−i) S3 alloy

grain size is ~85 μm by the first pass of rolling, and after the alloy is rolled for two passes, the grain size reaches ~50 μm. The S2 alloy grain size is refined to ~12 μm as the rolling reduction continues. It can be seen that the grain size increases with the increase in rolling temperature. In addition, a certain number of deformation twins are also found in the S2 alloy (as shown by the blue arrows in Figs. 5(e, f)).

The metallographic photographs of the S3 alloys at different magnifications are shown in Figs. 5(g, h, i). It is evident that the S3 alloy involves a high proportion of un-dynamic recrystallized (un-DRXed) regions, suggesting that the degree of dynamic recrystallization (DRX) in the S3 alloy is pretty low. The grain structure of the alloy exhibits a typical mixed grain structure, which contains deformed coarse grains (CG) and refined recrystallized grains (FG). The DRXed grains are mainly distributed near the original grain boundaries (GBs), which is related to the intensification of lattice mismatch and the increase of dislocation density near the GBs [33,34].

Similarly, a certain number of deformation twins are formed in the S3 alloy (as shown in Figs. 5(h, i)). The formation of deformation twins relates to the poor formability of magnesium alloys. For magnesium alloys with a hexagonal close-packed (HCP) structure, twinning is another important deformation mechanism besides slip. It can accommodate plastic deformation by inducing lattice reorientation and optimize the alloy microstructure by inducing DRX [35,36]. It is worth mentioning that the petal-like structure formed during the homogenization process still exists after rolling deformation.

The microstructure evolution of as-rolled WE54 alloys is characterized by EBSD, as shown in Fig. 6. After three passes of rolling at 450 °C, DRX occurs in the S1 alloy, and the DRXed grains are equiaxed with an average size of ~7.9 μm (as shown in Fig. 6(b)). The inverse pole figure in Fig. 6(a) shows that the S1 alloy exhibits a strong basal texture of $[0001]_{Mg}$//ND, and the maximum texture intensity is ~8.65. When the rolling temperature increases to 490 °C, DRX also takes

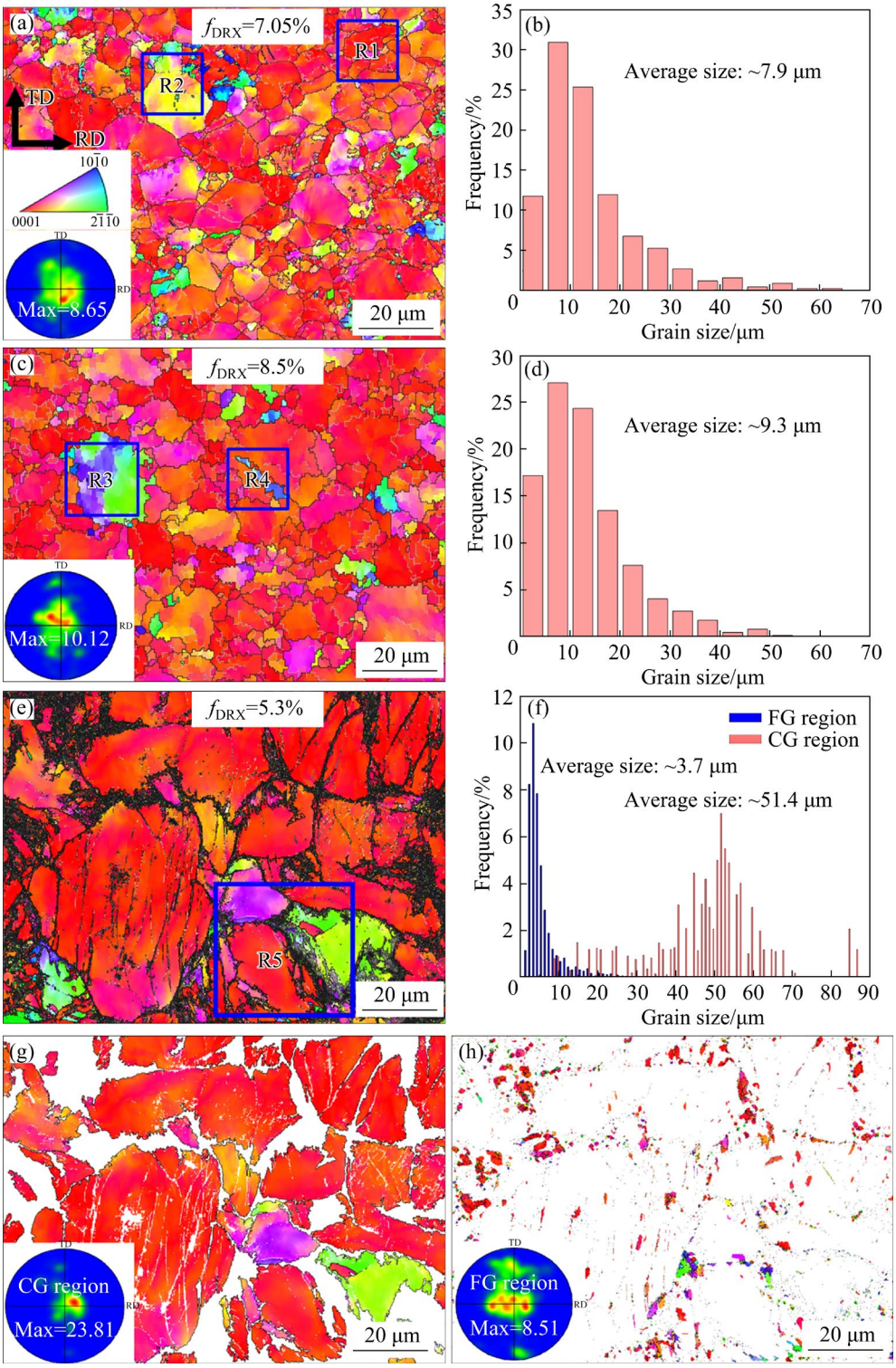


**Fig. 6** IPF figures, pole figures, and grain size distributions of as-rolled WE54 alloys: (a, b) S1 alloy; (c, d) S2 alloy; (e–h) S3 alloy

place in the S2 alloy, and the grain size for the S2 alloy is slightly increased compared with that of the S1 alloy, which is to be ~9.3 μm. The inverse pole figure of the S2 alloy also exhibits a strong basal texture, with a maximum texture intensity of ~10.12. When the alloy is HPRed at 490 °C with considerable reduction (65%) in a single pass, DRX only appears in the original GBs, and most of the regions are un-DRXed regions consisting of deformed CGs. The grain size statistics in Fig. 6(f)

shows that the grain size for the FG regions is ~3.7 μm, while the grain size in the CG regions reaches ~51.4 μm. The inverse pole figure of the CG regions shows that deformed CGs exhibit an extremely strong basal texture, with a maximum texture intensity of ~23.81, while the maximum texture intensity in FG regions is just ~8.51. The results indicate that the deformed grains rotate under stress, and their basal plane rotates to be parallel to the RD, thus forming a strong basal texture. In contrast, DRXed grains nucleate and grow up during the rolling process, and the grains are oriented more randomly, presenting a weak texture [37,38].

The DRX and deformed grains are separated by grain orientation spread (GOS), and the volume fraction of DRXed grains in different alloys was calculated. The results in Fig. 6 show that the fractions of DRXed grains in S1, S2 and S3 alloys are 7.05%, 8.5% and 5.3%, respectively, indicating that the fraction of DRXed grains increases moderately when the rolling temperature increases. After a considerable reduction in a single pass, the alloy mainly comprises CGs with a low proportion of DRXed grains. From the microstructure differences among S1, S2, and S3 alloys, the deformation behaviour of WE54 alloy is not only affected by the rolling temperature but also by the rolling path. The recrystallization and strengthening mechanisms of the WE54 alloy at different temperatures and rolling paths will be analyzed in detail below.

### 3.2 Mechanical properties of alloys at different states

The typical room-temperature tensile stress-strain curves and the corresponding mechanical properties of WE54 alloys at different states are presented in Fig. 7. Compared with the cast alloy, the mechanical properties of as-rolled alloys are significantly improved. The yield strength (YS), ultimate tensile strength (UTS), and elongation (EL) of as-cast WE54 alloy are ~123 MPa, ~207 MPa, and ~6.5%, respectively, while the as-rolled S1 alloy exhibits a YS of ~323 MPa, UTS of ~374 MPa, and elongation of ~5.0%. That is, the yield strength of WE54 alloy has improved more than twice, with almost no decrease in elongation, indicating that the strengthening effect of HPR is very significant. The mechanical properties of as-rolled S2 alloy exhibit YS of ~279 MPa, UTS of ~338 MPa, and elongation of ~8.0%. Compared to the S1 alloy, the strength of the as-rolled S2 alloy decreases, but its elongation is improved. The as-rolled S3 alloy exhibits better mechanical properties than the S2 alloy, with YS, UTS and EL of ~320 MPa, ~365 MPa and ~4.5%, respectively. The changes in mechanical properties of different alloys are related to the grain size, texture intensity, dislocation density, etc.

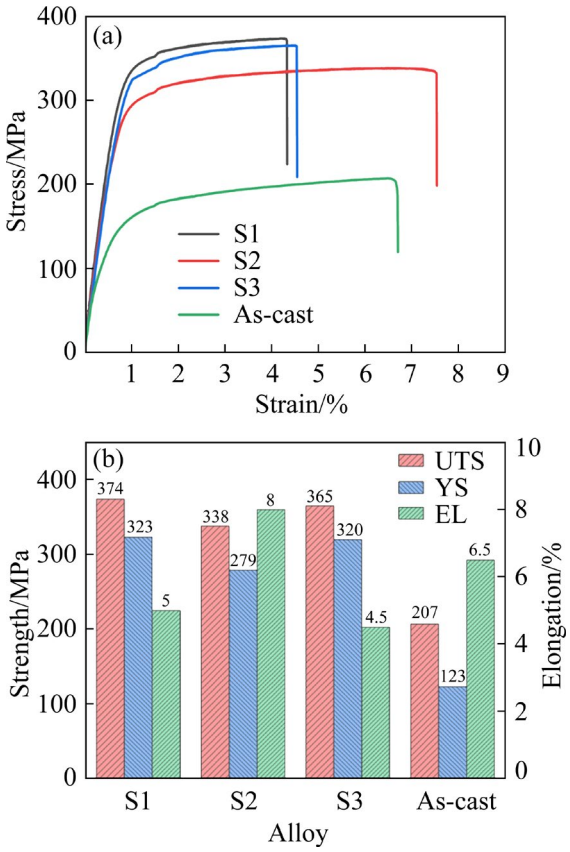


**Fig. 7** Room-temperature tensile stress−strain curves (a) and mechanical properties (b) for WE54 alloys at different states

Figure 8 shows SEM images of the tensile fracture surfaces of different as-rolled alloys. The fracture surfaces of all the rolled alloys are observed to have many cleavage planes and tearing ridges, as shown in Figs. 8(a, c, e), which is characterized by brittle fracture. Meanwhile, a certain number of dimples are also identified from the high-magnification images of Figs. 8(b, d, f), indicating that the fracture mode of the as-rolled alloys is a combination of the brittleness and toughness.

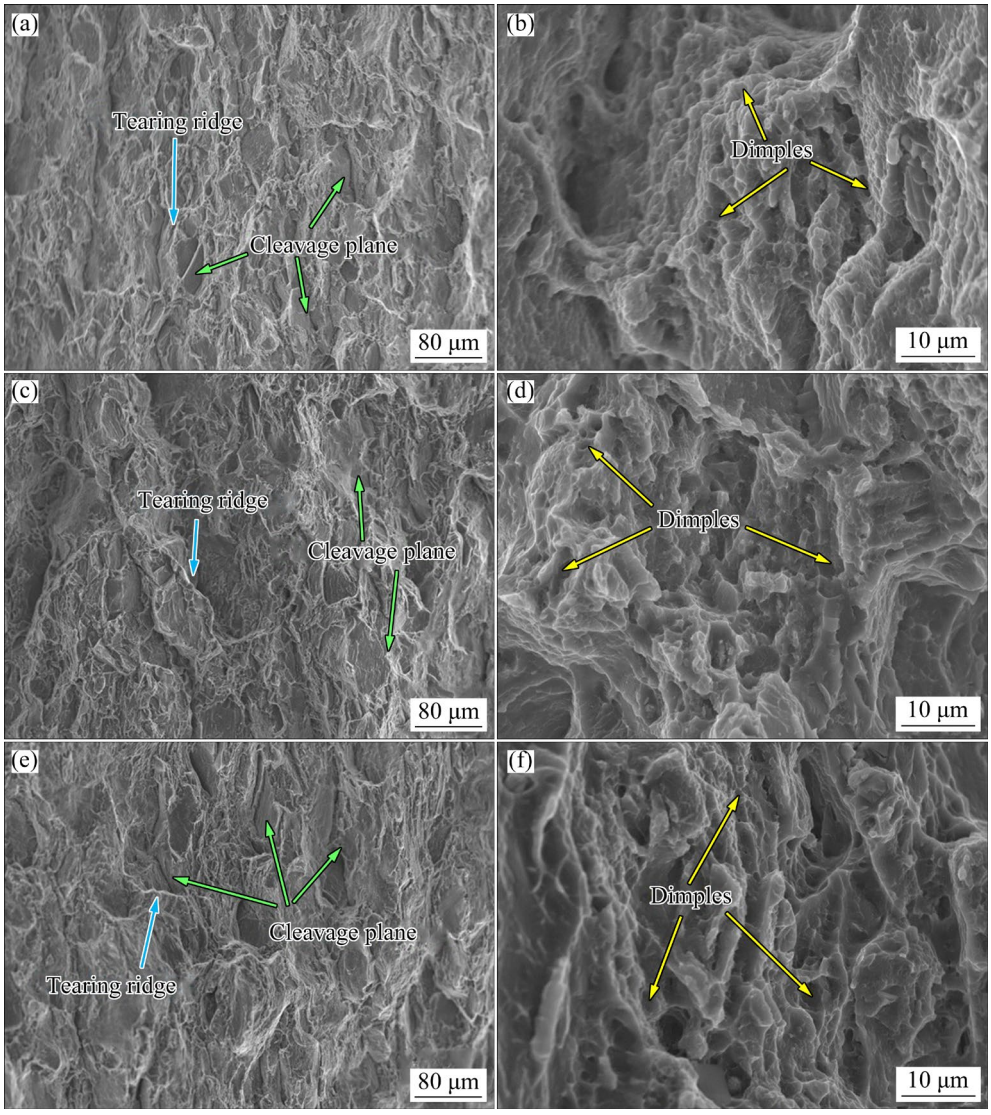


**Fig. 8** SEM images of tensile fracture surfaces for as-rolled WE54 alloys: (a, b) S1 alloy; (c, d) S2 alloy; (e, f) S3 alloy

## 4 Discussion

### 4.1 Recrystallization mechanisms of as-rolled WE54 alloys

During the HPR process, the WE54 alloy undergoes DRX to achieve grain refinement. To clarify the DRX mechanism of the alloy during different HPR processes, typical regions of as-rolled alloys in the final pass, i.e., the R1−R5 regions in Fig. 6, are selected for further analysis.

To analyze the DRX mechanism of as-rolled S1 alloy, R1 and R2 regions from Fig. 6(a) were selected. The EBSD results of the R1 region are shown in Fig. 9. It can be observed in Fig. 9(a) that the parent grains are divided by the DRXed grains and subgrain boundaries (sub-GBs), forming the unDRXed regions of $P_1$, $P_2$, and $P_3$, the DRXed grains of $G_1$−$G_6$, and the subgrain $S_1$. The parent grains show irregular shapes and serrated GBs. Sub-GBs isolate the subgrain S1 from its parent grains. New DRXed grains ($G_1$−$G_3$) are formed along the serrated GBs and at the triple junctions of the parent grains. The GBs of $P_1$ are bowed toward the adjacent grains, leading to the formation of $G_1$−$G_3$ grains. The above observations provide adequate evidence for the operation of the discontinuous dynamic recrystallization (DDRX) process with conventional nucleation and nucleus growth at serrated pre-existing high-angle grain boundaries (HAGBs) by bulging [39].

The line graph (Fig. 9(b)) represents the misorientation angle from point to origin and point to point along the arrow direction of A to B in $P_1$

grain (as shown by the black arrow in Fig. 9(a)). The line profile of point-to-origin suggests that the misorientation angle increases gradually up to ~14° as the distance increases, indicating the continuous change of orientation occurring in the $P_1$ grain, i.e., dislocations within the grain are pretty active. Figure 9(c) depicts the crystallographic orientations of different grains in the R1 region. It can be observed that grain orientations differ significantly between the DRXed grains and unDRXed grains, as the DRXed grains of $G_1$−$G_6$ have a random orientation. In contrast, unDRXed grains of $P_1$−$P_3$ have a basal orientation.

Figure 10 depicts the EBSD results of the R2 region. It is evident in Fig. 10(a) that DRXed grains such as $G_1$−$G_9$ are distributed at the parent GBs, surrounded by a high density of low-angle grain boundaries (LAGBs) and sub-GBs. Fine DRXed grains named $G_1$−$G_7$ in Fig. 10(a) are formed at the severe accumulation region of sub-GBs. It can be

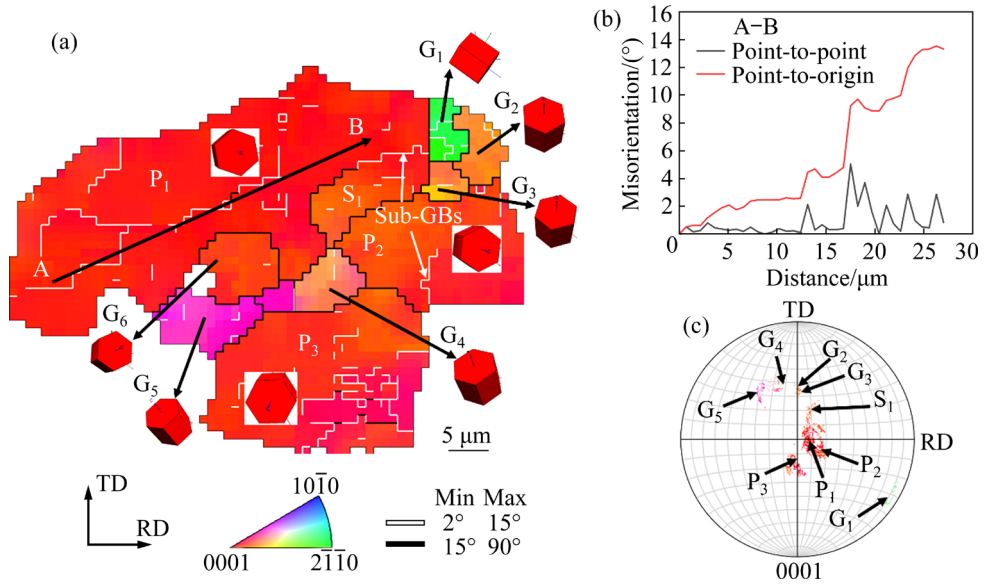


**Fig. 9** EBSD results of R1 region: (a) IPF figure; (b) Line graph of misorientation angle along arrow AB in (a); (c) (0001) pole figure

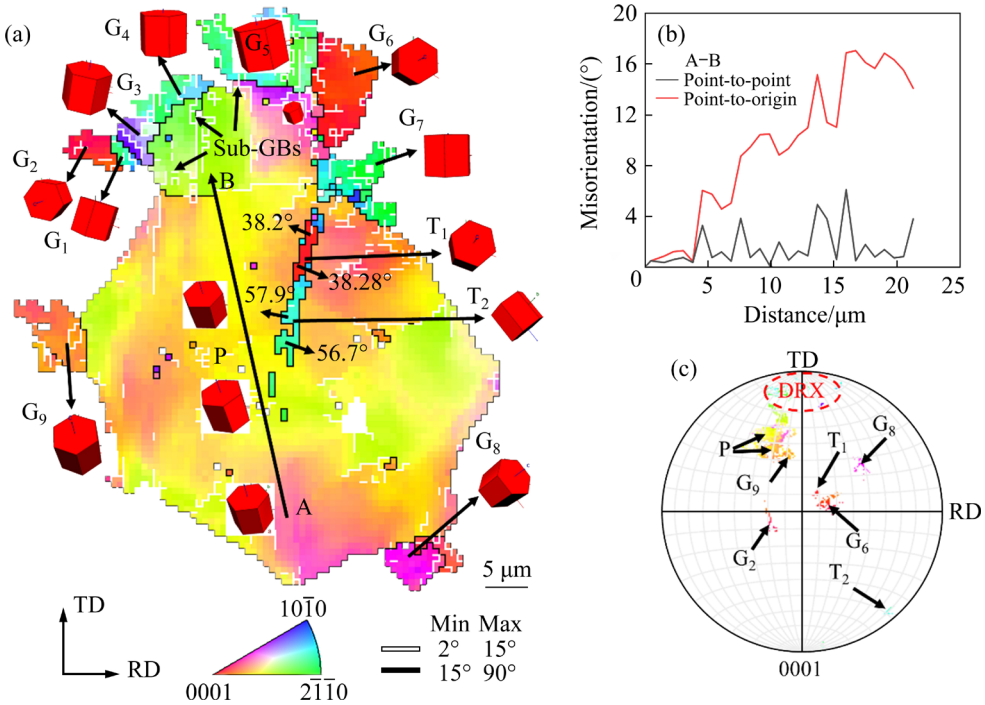


**Fig. 10** EBSD results of R2 region: (a) IPF figure; (a) Line graph of misorientation angle along arrow AB in (a); (c) (0001) pole figure

deduced that the nucleation of DRXed grains is related to the continuous absorption of dislocations in these sub-GBs. As the deformation continues, dislocations gradually accumulate and rearrange at the GBs, forming LAGBs. The LAGBs absorb the surrounding dislocations continuously and transform into the HAGBs; thus, new DRXed grains are formed. The formation of these DRXed grains is classified as a typical continuous dynamic recrystallization (CDRX) mechanism [39,40]. Double twins $\{10\bar{1}1\}-\{10\bar{1}2\}$ and contraction twins $\{10\bar{1}1\}$ (as shown by $T_1$ and $T_2$ in Fig. 10(a)) are observed in this region. The contraction twins reorient the crystal lattice by ~56.2° about $\langle 11\bar{2}0\rangle$ directions, and double twins $\{10\bar{1}1\}-\{10\bar{1}2\}$ have a reorientation by ~ 37.5° about the same direction [41,42]. During the deformation process, strain accumulation occurs inside the $\{10\bar{1}1\}$ contraction twins and the $\{10\bar{1}1\}-\{10\bar{1}2\}$ double twins with stable twin boundaries (TBs). The dislocations move inside TBs to form sub-GBs, which then transform into LAGBs and new DRXed grains are formed, referred to as the twin-induced recrystallization mechanism (TDRX) [40,42].

Figure 10(b) shows the misorientation distribution from point to origin and from point to point along the black arrow AB inside the parent grains P. It can be observed that the misorientation angle in the parent grain P increases with the increase of the distance. When the distance is ~20 μm, the point-to-origin misorientation angle increases to ~16°, indicating that the dislocation inside the parent grains is very active. The pole figure in Fig. 10(c) shows the orientation of grains in the R2 region. It can be seen that the orientation of the DRX grains ($G_1$, $G_3$−$G_5$, and $G_7$) (as shown by the red dashed line in Fig. 10(c)) is consistent with that of the parent grains, which is one of the typical characteristics of CDRX mechanism.

The R3 and R4 regions are selected to investigate the DRX mechanism of S2 alloys, and the EBSD results are shown in Fig. 11. For the R3 region in Fig. 11(a), it can be observed that the parent grains are divided into DRXed regions ($G_1$−$G_6$) and unDRXed regions ($P_1$, $P_2$ and $P_3$) by GBs. The simultaneous formation of DRXed $G_1$−$G_6$ with a high density of LAGBs at original GBs indicates that the CDRX also occurs in the R3 region. For the R4 region of Fig. 11(d), the parent grains also consist of unDRXed and DRXed regions located at GBs. Contraction twins $\{10\bar{1}1\}$ can also be observed in the R4 region, as shown by $T_1$ in Fig. 11(d), suggesting that the TDRX mechanism also occurs in S2 alloys. The misorientation distribution from point to origin and from point to point along the black arrows AB in the parent grains of P3 and P are presented in Figs. 11(b) and 11(e), respectively. As the distance increases to 35 μm, the point-to-origin misorientation angle in the parent grains gradually increases to ~20° and ~21°, respectively, indicating the high activity of dislocations in the S2 alloy. Figures 11(c, f) show the kernel average misorientation maps (KAM) of the R3 and R4 regions. It can be observed that both regions have high-density dislocations, which corresponds to the results in Figs. 11(b, e).

Figure 12 shows the EBSD analysis results of the R5 region. Inverse pole figure map in Fig. 12(a) exhibits a mixed-grain structure consisting of coarse unDRXed grains ($P_1$, $P_2$ and $P_3$) and relatively refined DRXed grains ($G_1$−$G_5$). The finer DRXed grains are formed both along the unDRXed GBs and within the grains, which is associated with the CDRX and TDRX mechanisms. Many LAGBs are distributed at the parent GBs, which can further migrate to form new DRXed grains. Examination of the KAM maps (Fig. 12(b)) indicates that the unDRXed grains have higher dislocation density at the original GBs compared to the intragranular regions. The accumulation of dislocations can provide energy for the subsequent DRX processes, which is the reason for the high density of LAGBs at the original GBs. Figure 12(c) shows the misorientation distribution from point to origin and from point to point along the black arrow AB in the $P_1$ grain. The point-to-origin misorientation angle in the parent grains gradually increases to ~19°, indicating the continuous orientation change in the parent grains.

### 4.2 Strengthening mechanisms of WE54 alloy

The mechanical properties of WE54 alloy are improved to different degrees compared with the as-cast state after the HPR deformation, as shown in Fig. 7. There are multiple reasons for the enhancement of WE54 alloy. Firstly, the DRX of the alloy occurs after the HPR deformation, and the grain is effectively refined, resulting in the fine-grain strengthening. The second is that the alloy has a high density of dislocations during the HPR

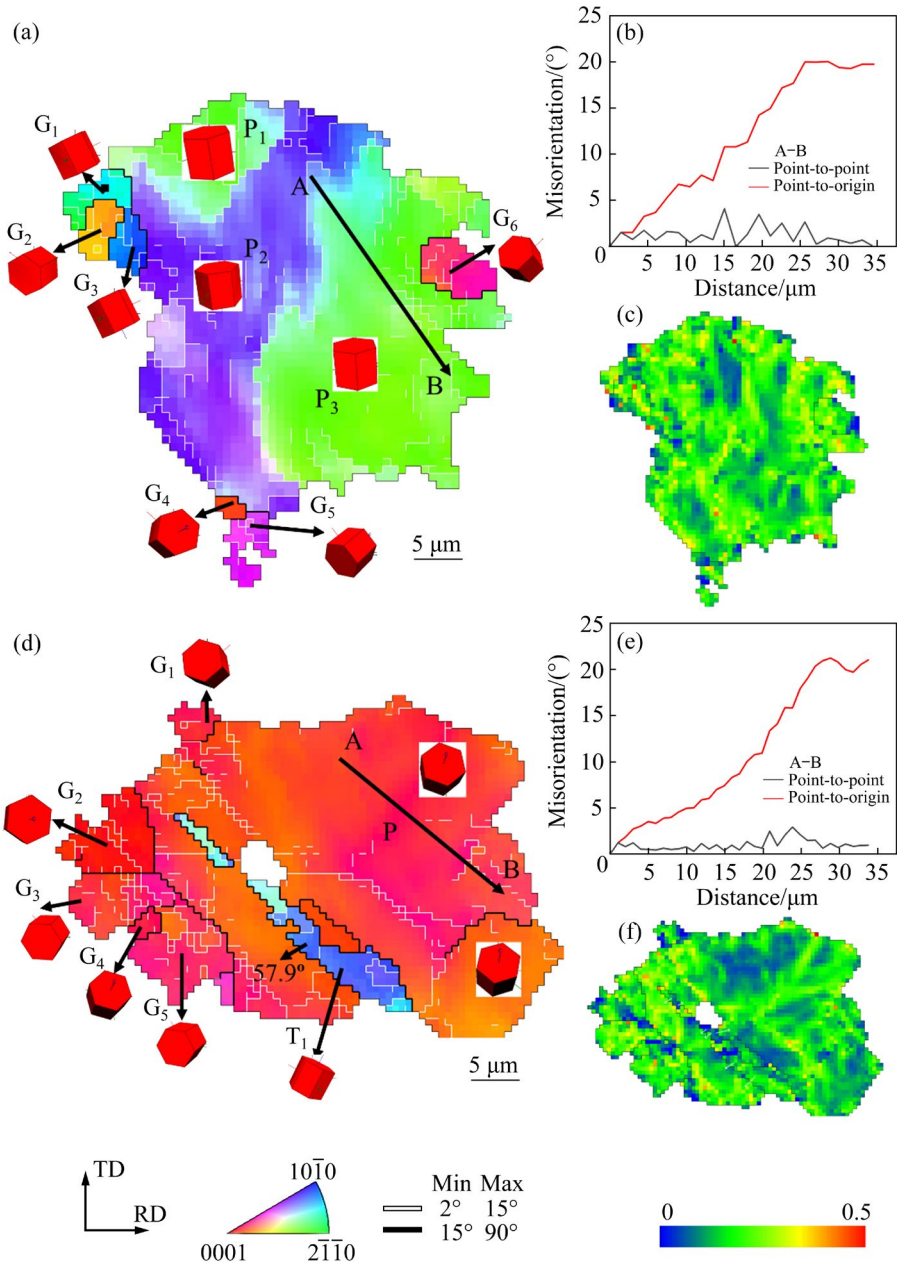


**Fig. 11** EBSD results of R3 (a−c) and R4 (d−f) regions: (a, d) IPF figures; (b, e) Line graphs of misorientation angle along arrows AB; (c, f) KAM maps

processes, and these dislocations generate work hardening. Moreover, the solid solution of Y, Nd elements can produce a strong strengthening effect. In addition, the twin boundaries and precipitation of the Zr phase can also contribute to the strengthening of the alloy.

High-density residual dislocations generated during the HPR process can be considered geometrically necessary dislocations (GNDs) [40]. The KAM method is used to study the GNDs in as-rolled WE54 alloys quantitatively. According to this method, the GNDs are determined by the local misorientation. Local misorientation angles below 5° measured by EBSD are considered to estimate the GNDs according to the formula:

$$\rho^{\mathrm{GNDs}} = \frac{2\Delta\theta_{\mathrm{i}}}{\mu b} \tag{1}$$

where $\rho^{\mathrm{GNDs}}$ stands for the GNDs density; $\Delta\theta_{\mathrm{i}}$ represents the local misorientation; $\mu$ is the step size of the EBSD map (1 μm); $b$ is the magnitude of Burgers vector ($3.2\times10^{-10}$ m in use) [43].

Figure 13 shows the KAM maps and the corresponding $\rho^{\mathrm{GNDs}}$ of as-rolled S1, S2, and S3

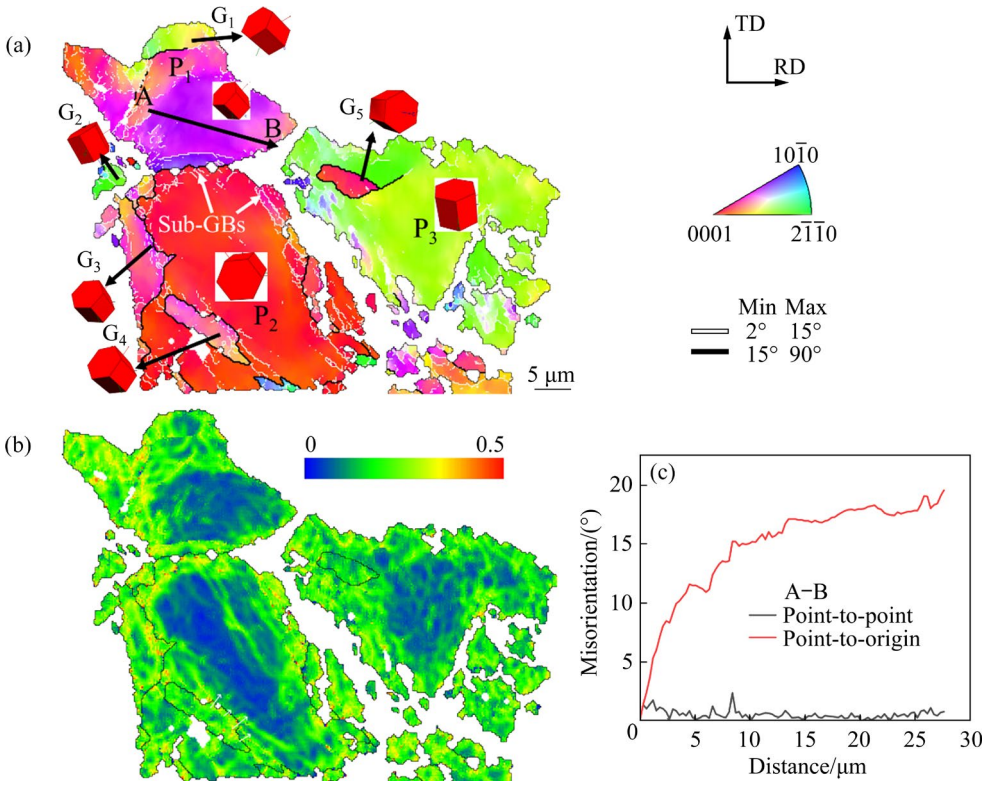


**Fig. 12** EBSD results of R5 region: (a) IPF figure; (b) KAM map; (c) Line graph of misorientation angle along arrow AB in (a)

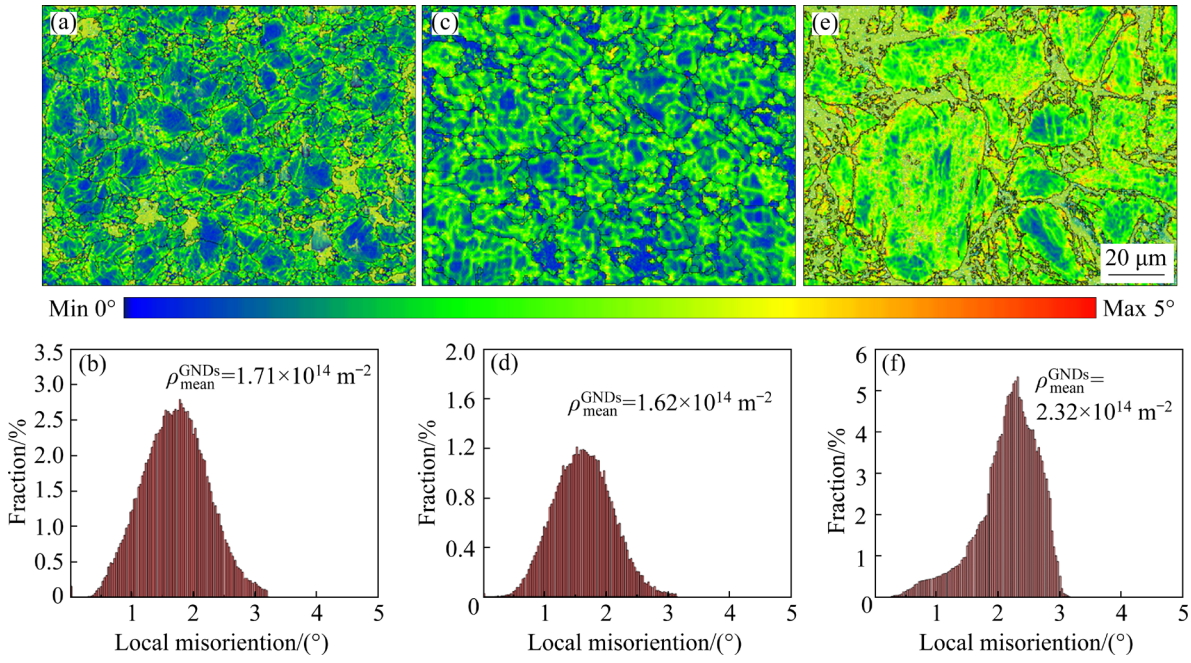


**Fig. 13** KAM maps (a, c, e) and corresponding local misorientation angle distribution maps (b, d, f) for as-rolled WE54 alloys: (a, b) S1 alloy; (c, d) S2 alloy; (e, f) S3 alloy

alloys. The calculated $\rho^{GNDs}$ values for the as-rolled S1, S2, and S3 alloys are ~1.71×10$^{14}$, ~1.62×10$^{14}$, and ~2.32×10$^{14}$ m$^{-2}$, respectively. When the rolling temperature increases, the dislocation density for the as-rolled S2 alloy decreases compared to the S1 alloy due to the consumption of DRXed grains. The grain sizes of the S1 and S2 alloys are close, and the Zr phase contents are at the same level.

However, the mechanical properties of the S1 alloy show a much better performance than those of the S2 alloy, which suggests that the high density of dislocations in the S1 alloy improves the level of its work-hardening.

In addition, there are more twin boundaries in S1 alloy, as shown in Fig. 5, which may give it higher mechanical properties. Twin boundaries can effectively impede dislocation movement and accelerate the accumulation of dislocations, providing an effect similar to that of fine-grain strengthening [44]. For the as-rolled S3 alloy, the single-pass rolling with a 65% thickness reduction results in dislocation accumulation. This is why the S3 alloy has higher mechanical properties despite larger grains. Furthermore, the significantly strong basal texture of the CGs also accounts for the increase in strength as well as the decrease in ductility of the S3 alloy [45].

For a better understanding of the strengthening mechanism of as-rolled alloys, the origin of yield strength of the S1 alloy is analyzed quantitatively. The yield strength ($\sigma_{ys}$) of the S1 alloy can be summarized as

$$\sigma_{ys}=\sigma_g+\sigma_d+\sigma_s+\sigma_{twin}+\sigma_p \quad (2)$$

where $\sigma_g$ represents the fine-grain strengthening, $\sigma_d$ represents the stress resulting from dislocation strengthening, $\sigma_s$ represents the solid solution strengthening, $\sigma_{twin}$ represents the stress arising from twin boundaries, and $\sigma_p$ represents the precipitation strengthening.

The fine-grain strengthening can be calculated using the following formula [44,46]:

$$\sigma_g=\sigma_0+kd^{-1/2} \quad (3)$$

where $\sigma_0$ and $k$ are the material constants, and the $\sigma_0$ and $k$ values of 50.7 MPa and 252 MPa·μm$^{1/2}$ are taken in this study [47]; $d$ is the average grain size (~7.9 μm). As a result, the calculated yielding strength due to grain refinement is ~140 MPa.

The dislocation strengthening can be evaluated by the Taylor formula [44]:

$$\sigma_d=M\alpha Gb\sqrt{\rho} \quad (4)$$

where $M$ is Taylor factor (taken as ~4.2 [48]), $\alpha$ is the coefficient with the value of 0.2, and the shear modulus $G$ is 17 GPa, and $\rho$ is the dislocation density. The calculated dislocation strengthening value is ~60 MPa.

Furthermore, the strengthening effect of solid solution atoms can be evaluated as follows [44]:

$$\sigma_s=MG\frac{\varepsilon_s^{3/2}c^{1/2}}{700} \quad (5)$$

where $\varepsilon_s$ is an experimental constant (taken as 0.74 [44]), and $c$ is the solute concentration in atomic fraction (The $c$ value is the sum of the atomic fractions of Y, Gd, and Nd elements in Table 2, which is 1.98 at.%). Therefore, the contribution of solid solution strengthening is ~64 MPa.

Therefore, the total contribution of the above strengthening mechanisms in the S1 alloy is 264 MPa, which is 59 MPa away from the measured yield strength of 323 MPa, indicating that the combined contribution of twin strengthening and precipitation strengthening is ~59 MPa. The WE54 magnesium alloy can obtain good mechanical properties after HPR deformation. This is due to the synergistic effect of fine grain strengthening, dislocation hardening, twin strengthening, and precipitation strengthening.

## 5 Conclusions

(1) After homogenization treatment at 525 °C for 8 h, the Mg−RE phases in WE54 alloy are decomposed, and a petal-like halo structure consisting of rod-shaped Zr phases with different length-to-diameter ratios precipitates.

(2) When the HPR temperature is 450 °C, the alloy grain is refined due to the dynamic recrystallization and a basal texture of $[0001]_{Mg}$// ND is formed. When the rolling temperature increases to 490 °C, the DRXed grain size increases slightly, and the dislocation density decreases. A mixed-grain structure is formed after a single pass rolling with a reduction of 65% at 490 °C.

(3) After three passes of HPR at 450 °C, the WE54 alloy has the best mechanical properties with a yield strength of 323 MPa, a tensile strength of 374 MPa, and an elongation of 5.0%. The grain refinement and the high-density dislocations are the main reasons for improving its mechanical properties.

(4) The dynamic recrystallization mechanisms of the WE54 alloy during HPR is a synergistic effect of discontinuous dynamic recrystallization, continuous dynamic recrystallization, and twin-induced recrystallization.

## CRediT authorship contribution statement

**Yan-hui LIU:** Conceptualization, Methodology, Investigation, Writing − Original draft, Writing − Review & editing; **Ming-ming QI**, **Xin CAO** and **Bing WU:** Data curation; **Ming LIANG** and **Jian-feng LI:** Supervision; **Chao LI:** Resources.

## Declaration of competing interest

The authors declare that they have no known competing financial interests or personal relationships that could have appeared to influence the work reported in this paper.

## Acknowledgments

This work was financially supported by the Natural Science Basic Research Program of Shaanxi Province, China (No. 2023-JC-QN-0581) and Advanced Power Specialty, China (No. YK22C-9).

## References

[1] HAN Xiu-zhu, HU Li, JIA Dong-yong, CHEN Jia-ming, ZHOU Tao, JIANG Shu-yong, TIAN Zheng. Role of unusual double-peak texture in significantly enhancing cold rolling formability of AZ31 magnesium alloy sheet [J]. Transactions of Nonferrous Metals Society of China, 2023, 33(8): 2351−2364.

[2] SONG Jiang-feng, SHE Jia, CHEN Dao-lun, PAN Fu-sheng. Latest research advances on magnesium and magnesium alloys worldwide [J]. Journal of Magnesium Alloys, 2020, 8(1): 1−41.

[3] ZHONG Li-ping, WANG Yong-jian. Evolution of precipitate orientation and its effect on thermal conductivity of Mg−5Sn alloy [J]. Transactions of Nonferrous Metals Society of China, 2023, 33(6): 1701−1714.

[4] CHAUDRY U M, HAMAD K, KIM J G. On the ductility of magnesium based materials: A mini review [J]. Journal of Alloys and Compounds, 2019, 792: 652−664.

[5] OVRI H, MARKMANN J, BARTHEL J, KRUTH M, DIERINGA H, LILLEODDEN E T. Mechanistic origin of the enhanced strength and ductility in Mg−rare earth alloys [J]. Acta Materialia, 2023, 244: 118550.

[6] LI Qian-kun, YAN Hong, CHEN Rong-shi. Effect of rolling reduction on deformation mechanism and twinning behavior of WE43 magnesium alloy [J]. Transactions of Nonferrous Metals Society of China, 2022, 32(12): 3901−3913.

[7] FATEMI S M, MORADIPOUR Y. Deformation mechanisms during continuous cooling compression of WE54 magnesium alloy [J]. Journal of Alloys and Compounds, 2020, 849: 156638.

[8] YU Zi-Jian, XU Xi, SHI Kang, DU Bao-tian, HAN Xiu-zhu, XIAO Tao, LI Shu-bo, LIU Ke, DU Wen-bo. Development and characteristics of a low rare-earth containing magnesium alloy with high strength-ductility synergy [J]. Journal of Magnesium Alloys, 2023, 11(5): 1629−1642.

[9] LI Ji-lin, CHEN Rong-shi, MA Yue-qun, KE Wei. Effect of Zr modification on solidification behavior and mechanical properties of Mg−Y−RE (WE54) alloy [J]. Journal of Magnesium and Alloys, 2013, 1(4): 346−351.

[10] GUI Yun-wei, CUI Yu-jie, BIAN Hua-kang, LI Quan-an, OUYANG Ling-xiao, CHIBA A. Deformation behavior of Mg−5Y−2Nd−0.5Zr alloys with different Sm additions [J]. Journal of Alloys and Compounds, 2020, 856: 158201.

[11] TIAN Zheng, YANG Qiang, GUAN Kai, MENG Jian, CAO Zhan-yi. Microstructure and mechanical properties of a peak-aged Mg−5Y−2.5Nd−1.5Gd−0.5Zr casting alloy [J]. Journal of Alloys and Compounds, 2018, 731: 704−713.

[12] OROZCO-CABALLERO A, ALVAREZ-LEAL M, RUANO O A, FERNANDO CARRE ÑO F. Improving the mechanical properties of a WE54 magnesium alloy through severe friction stir processing and rapid cooling [J]. Materials Science and Engineering A, 2022, 856: 143963.

[13] ZHOU Meng-ran, HUANG Xin-sheng, MORISADA Y, FUJJI H, CHINO Y. Effects of Ca and Sr additions on microstructure, mechanical properties, and ignition temperature of hot-rolled Mg−Zn alloy [J]. Materials Science and Engineering A, 2020, 769: 138474.

[14] WANG Hui-yuan, YU Zhao-peng, ZHANG Lei, LIU Chun-guo, ZHA Min, JIANG Qi-chuan. Achieving high strength and high ductility in magnesium alloy using hard-plate rolling (HPR) process [J]. Scientific Reports, 2015, 5(1): 17100.

[15] ZHA Min, ZHANG Xuan-he, ZHANG Hang, YAO Jia, WANG Cheng, WANG Hui-yuan, FENG Ting-ting, JIANG Qi-chuan. Achieving bimodal microstructure and enhanced tensile properties of Mg−9Al−1Zn alloy by tailoring deformation temperature during hard plate rolling (HPR) [J]. Journal of Alloys and Compounds, 2018, 765: 1228−1236.

[16] ZHANG Hang, WANG Hui-yuan, WANG Jin-guo, RONG Jian, ZHA Min, WANG Cheng, MA Pin-kui, JIANG Qi-chuan. The synergy effect of fine and coarse grains on enhanced ductility of bimodal-structured Mg alloys [J]. Journal of Alloys and Compounds, 2019, 780: 312−317.

[17] SANYAL S, BHUYAN P, BANDYOPADHYAY T K, MANDAL S. Insights into the effect of different thermo-mechanical processing on the microstructure, phases, texture and tensile properties in Mg−0.9Al−0.6Mn−0.2Si−0.1Ca alloy [J]. Intermetallics, 2022, 146: 107564.

[18] SANYAL S, BHUYAN P, BANDYOPADHYAY T K, MANDAL S. Multiscale precipitate evolution and its implications on the tensile deformation behavior in thermo-mechanically processed and peak-aged lean Mg−Al−Ca−Mn alloy [J]. Materialia, 2022, 26: 101566.

[19] SANYAL S, KANODIA S, SAHA R, BANDYOPADHYAY T K, MANDAL S. Influence of hard plate hot forging temperature on the microstructure, texture and mechanical properties in a lean Mg−Zn−Al alloy [J]. Journal of Alloys and Compounds, 2019, 800: 343−354

[20] DULEY P, SANYAL S, BANDYOPADHYAY T K, MANDAL S. Implications of annealing treatments on microstructure, texture, and tensile properties of hard plate hot forged Mg−Zn−Ca−Mn alloy [J]. Materials Characterization, 2021, 172: 110885.

[21] DULEY P, SANYAL S, BANDYOPADHYAY T K,

MANDAL S. Implications of grain size distribution, precipitate evolution and texture development on tensile properties in hard plate hot forged and annealed Mg−Zn−Ca−Mn alloy [J]. Materials Science and Engineering A, 2020, 784: 139288.

[22] ZHANG M, ZHANG W Z. Interpretation of the orientation relationship and habit plane orientation of the equilibrium $\beta$-phase in an Mg−Y−Nd alloy [J]. Scripta Materialia, 2008, 59(7): 706−709.

[23] WANG Li-dong, XING Cheng-yao, HOU Xiu-li, WU Yao-ming, SUN Jian-fei, WANG Li-min. Microstructures and mechanical properties of as-cast Mg−5Y−3Nd−Zr−$x$Gd ($x$=0, 2 and 4 wt.%) alloys [J]. Materials Science and Engineering A, 2010, 527: 1891−1895.

[24] CHEN Xian-hua, GENG Yu-xiao, PAN Fu-sheng. Microstructure, mechanical properties and electromagnetic shielding effectiveness of Mg−Y−Zr−Nd alloy [J]. Rare Metal Materials and Engineering, 2016, 45(1): 13−17.

[25] KIANI F, LIN Ji-xing, VAHID A, MUNIR K, WEN C, LI Yun-cang. Mechanical and corrosion properties of extruded Mg−Zr−Sr alloys for biodegradable implant applications [J]. Materials Science and Engineering A, 2022, 831: 142192.

[26] ZHAO Tian-shuo, HU Yao-bo, ZHANG Chao, HE Bing, ZHENG Tian-xu, TANG Ai-tao, PAN Fu-sheng. Influence of extrusion conditions on microstructure and mechanical properties of Mg−2Gd−0.3Zr magnesium alloy [J]. Journal of Magnesium Alloys, 2022, 10(2): 420−433.

[27] TONG Xin, WU Guo-hua, EASTON M A, SUN Ming, STJOHN D H, JIANG Rui, QI Fang-zhou. Exceptional grain refinement of Mg−Zr master alloy treated by tungsten inert gas arc re-melting with ultra-high frequency pulses [J]. Scripta Materialia, 2022, 215: 114700.

[28] WU Guo-hua, WANG Cun-long, SUN Ming, DING Wen-jiang. Recent developments and applications on high-performance cast magnesium rare-earth alloys [J]. Journal of Magnesium and Alloys, 2020, 9(1): 1−20.

[29] ZHANG Zhen-yan, PENG Li-ming, ZENG Xiao-qin, FU Peng-huai, DING Wen-jiang. Characterization of phases in a Mg−6Gd−4Sm−0.4Zr (wt.%) alloy during solution treatment [J]. Materials Characterization, 2009, 60: 555−559.

[30] HU Yao-bo, DENG Juan, ZHAO Chong, WANG Jing-feng, PAN Fu-sheng. Microstructure and mechanical properties of as-quenched Mg−Gd−Zr alloys [J]. Transactions of Nonferrous Metals Society of China, 2011, 21(4): 732−738.

[31] XIE He, WU Guo-hua, ZHANG Xiao-long, LI Zhong-quan, LIU Wen-cai, ZHANG Liang, SUN Bao-de. Microstructural evolution and mechanical performance of cast Mg−3Nd−0.2Zn−0.5Zr alloy with Y additions [J]. Transactions of Nonferrous Metals Society of China, 2022, 32(10): 3222−3237.

[32] XIAO Lei, YANG Guang-yu, MA Jia-qi, QIN He, LI Jie-hua, JIE Wan-qi. Microstructure evolution and fracture behavior of Mg−9.5Gd−0.9Zn−0.5Zr alloy subjected to different heat treatments [J]. Materials Characterization, 2020, 168: 110516.

[33] PENG Peng, ZHANG Kun-ming, SHE Jia, TANG Ai-tao, ZHANG Jian-yue, SONG Kai, YANG Qing-shan, PAN Fu-sheng. Role of second phases and grain boundaries on dynamic recrystallization behavior in ZK60 magnesium alloy [J]. Journal of Alloys and Compounds, 2020, 861: 157958.

[34] JIANG M G, XU C, NAKATA T, YAN H, CHEN R S, KAMADO S. Development of dilute Mg−Zn−Ca−Mn alloy with high performance via extrusion [J]. Journal of Alloys and Compounds, 2016, 668: 13−21.

[35] XU C, NAKATA T, QIAO X G, JIANG H S, SUN W T, CHI Y C, ZHENG M Y, KAMADO S. Effect of extrusion parameters on microstructure and mechanical properties of Mg−7.5Gd−2.5Y−3.5Zn−0.9Ca−0.4Zr (wt.%) alloy [J]. Materials Science and Engineering A, 2017, 685: 159−167.

[36] ZHANG Qian, LI Quan-an, CHEN Xiao-ya, ZHAO Jia-xin, BAO Jian, CHEN Zi-yi. Dynamic precipitation and recrystallization mechanism during hot compression of Mg−Gd−Y−Zr alloy [J]. Journal of Materials Research & Technology, 2021, 15: 37−51.

[37] LI Jing-li, DONG Zhao-hui, YI Xin, WU Di, CHEN Rong-shi. Twin evolution in cast Mg−Gd−Y alloys and its dependence on aging heat treatment [J]. Journal of Magnesium and Alloys, 2023, 11(7): 2285−2298.

[38] LI Lian-hui, LIU Wen-hong, QI Fu-gang, WU Di, ZHANG Zhi-qiang. Effects of deformation twins on microstructure evolution, mechanical properties and corrosion behaviors in magnesium alloys—A review [J]. Journal of Magnesium and Alloys, 2022, 10(9): 2334−2353.

[39] JIANG M G, XU C, YAN H, FAN G H, NAKATA T, LAO C S, CHEN R S, KAMADO S, HAN E H, LU B H. Unveiling the formation of basal texture variations based on twinning and dynamic recrystallization in AZ31 magnesium alloy during extrusion [J]. Acta Materialia, 2018, 157: 53−71.

[40] LI Qian-kun, YAN Hong, LIU Hong-hui, CHEN Rong-shi. Dynamic recrystallization mechanism and near-isotropic mechanical properties of WE43 magnesium alloy sheets rolled at different temperatures [J]. Materials Characterization, 2022, 193: 112259.

[41] KNEZEVIC M, LEVINSON A, HARRIS R, MISHRA R K, DOHERTY R D, KALIDINDI S R. Deformation twinning in AZ31: Influence on strain hardening and texture evolution [J]. Acta Materialia, 2010, 58: 6230−6242.

[42] HUANG Xin-de, XIN Yun-chang, CAO Yu, LI Wei, HUANG Guang-jie, ZHAO Xi, LIU Qing, WU Pei-dong. Understanding the mechanisms of texture evolution in an Mg−2Zn−1Ca alloy during cold rolling and annealing [J]. International Journal of Plasticity, 2022, 158: 103412.

[43] PENG Peng, She Jia, YANG Qing-shan, LONG Shuai, TANG Ai-tao, ZHANG Jian-yue, DAI Qing-wei, PAN Fu-sheng. Bimodal grained Mg−0.5Gd−$x$Mn alloys with high strength and low-cost fabricated by low-temperature extrusion [J]. Journal of Alloys and Compounds, 2023, 935: 168008.

[44] YANG Yu-liang, LIU Yu-xin, JIANG Shuang, YUAN Ye, CHEN Wei-ye, SUN Li-fang, HE Zhu-feng, ZHAO Xiao-li, JIA Nan. Achieving exceptional strength and ductility combination in a heterostructured Mg−Y alloy with densely refined twins [J]. Journal of Materials Science & Technology, 2024, 189: 132−145.

[45] WANG H, ZHANG D T, Qiu C, ZHANG W W, CHEN D L. Achieving superior mechanical properties in a low-alloyed magnesium alloy via low-temperature extrusion [J]. Materials Science and Engineering A, 2022, 851: 143611.

[46] PAN Hu-cheng, KANG Rui, LI Jing-ren, XIE Hong-bo, ZENG Zhuo-ran, HUANG Qiu-yan, YANG Chang-lin, REN Yu-ping, QIN Gao-wu. Mechanistic investigation of a low-alloy Mg−Ca-based extrusion alloy with high strength−ductility synergy [J]. Acta Materialia, 2020, 186: 278−298.
[47] SOMEKAWA H, MUKAI T. Hall−Petch relation for deformation twinning in solid solution magnesium alloys [J]. Materials Science and Engineering A, 2013, 561: 378−385.
[48] SHEN J H, LI Y L, WEI Q. Statistic derivation of Taylor factors for polycrystalline metals with application to pure magnesium [J]. Materials Science and Engineering A, 2013, 582: 270−275.

# WE54 镁合金在衬板轧制过程中的显微组织演变和强化机制

刘艳辉[1]，祁明明[2]，曹 鑫[1]，吴 冰[1]，梁 明[1]，李建峰[1]，李 超[1]

1．西北有色金属研究院 镁锂材料研究所，西安 710016；
2．西安理工大学 材料科学与工程学院，西安 710048

**摘 要**：对 WE54 镁合金在不同衬板轧制工艺下的显微组织演变及强韧化机制进行系统研究。结果表明，轧制态 WE54 合金的力学性能相比铸态大幅提升。在 450 ℃和 490 ℃下经过三道次轧制后，合金晶粒由于发生动态再结晶而细化。490 ℃下单道次大变形(65%)后，合金中形成了混晶组织。WE54 合金在衬板轧制过程中的动态再结晶机制为连续动态再结晶(CDRX)、不连续动态再结晶(DDRX)以及孪晶诱导再结晶(TDRX)。在 450 ℃下经三道次变形后的 WE54 合金具有最高的强度，其抗拉强度(UTS)与屈服强度(TYS)分别为 374 MPa 与 323 MPa。合金力学性能显著提高的原因在于细晶强化、固溶强化以及位错强化。

**关键词**：WE54 合金；衬板轧制；显微组织；力学性能；强化机制

**(Edited by Bing YANG)**